Quantum-ready microwave detection with scalable graphene bolometers in the strong-localization regime

Editors' Suggestion

Quantum-ready microwave detection with scalable graphene bolometers in the strong-localization regime

Yu-Cheng Chang,[1,*] Federico Chianese,[2] Naveen Shetty,[2] Johanna Uden,[2] Aditya Jayaraman,[2] Joonas T. Peltonen,[1] Samuel Lara-Avila,[2] Bayan Karimi,[1,3] Andrey Danilov,[2] Jukka P. Pekola,[1] and Sergey Kubatkin[2,4,†]

[1] *Pico Group, QTF Centre of Excellence, Department of Applied Physics, Aalto University, P.O. Box 15100, FI-00076 Aalto, Finland*

[2] *Department of Microtechnology and Nanoscience, Chalmers University of Technology, 412 96 Gothenburg, Sweden*

[3] *Pritzker School of Molecular Engineering, University of Chicago, Chicago, Illinois 60637, USA*

[4] *InstituteQ—The Finnish Quantum Institute, Aalto University, P.O. Box 15100, FI-00076 Aalto, Finland*

(Received 7 July 2025; revised 30 March 2026; accepted 28 April 2026; published 2 June 2026)

Exploiting quantum interference of charge carriers, epitaxial graphene grown on silicon carbide emerges as a game-changing platform for ultrasensitive bolometric sensing, featuring an intrinsic resistive thermometer response unmatched by any other graphene variant. By achieving low and uniform carrier densities, we have accessed a regime of strong charge localization that dramatically reduces thermal conductance, significantly enhancing bolometer performance. Here we present scalable graphene-based bolometers engineered for detecting gigahertz-range photons, a frequency domain essential for superconducting quantum processors. Our devices deliver a state-of-the-art noise equivalent power of 40 $zW/\sqrt{Hz}$ at $T = 40$ mK, enabled by the steep temperature dependence of thermal conductance, $G_{th} \sim T^4$ for $T < 100$ mK. These results establish epitaxial graphene bolometers as versatile and low-backaction detectors, unlocking new possibilities for next-generation quantum processors and pioneering investigations into the thermodynamics and thermalization pathways of strongly entangled quantum systems.

DOI: 10.1103/pyd2-stcl

I. INTRODUCTION

Detecting extremely small powers of electromagnetic radiation is essential in modern physics, where even the faintest signals can carry valuable information. One prominent example is the search for axions—hypothetical particles that could make up dark matter—which undergo conversion into photons in a magnetic field, thus producing an extremely weak microwave radiation [1–3]. Another example is quantum information processing, where operations on qubits often involve single-photon or few-photon signals that require precise, low-noise detection. In both cases, bolometers provide an effective solution, extending to the opportunity of a single-shot readout of the qubit state [4–8]. These devices are temperature-dependent resistors that absorb radiation and are weakly thermally coupled to a reservoir, allowing them to register minute temperature increases. This enables accurate detection of tiny power levels without adding significant electrical noise. In a bolometer, minimizing electron-phonon coupling to the substrate is crucial to ensure that absorbed radiation effectively heats the electron system without rapidly dissipating energy to the lattice.

Graphene doped to the Dirac point is an ideal material for sensitive detection because a shrinking Fermi surface at extremely low electron density imposes phase-space restrictions for electron-phonon interactions. This allows graphene to retain absorbed energy for longer, resulting in higher temperature sensitivity and improved performance for detecting extremely small power levels. However, at high carrier density, graphene's intrinsic temperature dependence of resistivity is too weak for efficient bolometer operation [9,10]. To address this limitation, one can induce superconductivity in graphene by coupling it to a nearby superconductor and leverage the superconducting transition. Indeed, impressive results were achieved on a superconductor-graphene hybrid junction, with the use of an exfoliated graphene flake insulated by hexagonal

*Contact author: yu-cheng.chang@aalto.fi

†Contact author: sergey.kubatkin@chalmers.se

boron nitride [11]. Open issues that remain in this approach include scalability and, importantly, extending the operational temperature range of the proximitized-graphene bolometer, which is bound to operate close to the superconducting transition in the superconductor.

Here we overcome these two critical shortcomings by introducing a platform based on epitaxial graphene grown on silicon carbide, a wafer-scale technology, allowing uniform graphene doping close to the Dirac point [12]. In this system, the graphene layer exhibits an intrinsic temperature dependence of resistance caused by quantum interference of carriers in the presence of strong intervalley scattering [13–15]—a mechanism fundamentally different from superconducting proximity effects. Crucially, this response is not bound by a superconducting critical temperature; instead, device sensitivity increases continuously as temperature decreases, making it exceptionally well suited as a sensitive cryogenic radiation detector. We demonstrate that below 200 mK, quantum interference effects in graphene induce strong localization of charge carriers, pushing the graphene bolometer into a qualitatively new transport regime. This leads to a remarkable increase in both responsivity and thermal isolation from the reservoir, with the potential to enable unprecedented sensitivity of truly scalable graphene detectors.

Importantly, the graphene sensor presented has an extremely low heat capacity approaching that of a single degree of freedom, which translates into projected energy resolution in calorimeter mode, envisioned in Ref. [16], as low as $k_B T \simeq 0.7$ yJ $= 0.7 \times 10^{-24}$ J at 50 mK. Thus, it would provide a click-detector resolving a single photon with frequency above 1 GHz, which is a component of the future quantum information processing toolbox that has long been desired. Thanks to drastically different physical mechanisms behind bolometric operation as compared with previous reports of graphene-based detectors, our devices perform at the state-of-the-art level, making them promising for applications in quantum information processing with superconducting qubits operating in the gigahertz range, and for fundamental studies in this field.

II. SAMPLE DESIGN AND EXPERIMENTAL SETUP

We have fabricated a wafer with 16 graphene strips with different aspect ratios, and three Hall bars, aimed at evaluating transport properties of graphene (the chip layout is shown in Fig. 5 in Appendix A). To thermally isolate graphene, the current leads were made of aluminum, a superconductor with T_c of about 1 K. Contacts were fabricated with an edge-contact geometry [17], with use of 5 nm titanium as an adhesion layer. Hall bar measurements confirmed the targeted carrier density n of approximately 10^{10} electrons/cm^2, achieved by polymer-molecular doping [18]. Magnetotransport data for the longitudinal resistance hinted that localization in graphene is caused by quantum interference effects, which can be eliminated by application of a modest magnetic field, breaking time-reversal symmetry (see Fig. 7 in Appendix B). We conclude that upon lowering of the electron temperature, the quantum-mechanical interference of the charge carriers in graphene increases, and sets graphene in the strong-localization regime, where effects of electron-electron interactions further contribute to a steeper temperature dependence of R.

In this article we focus on the performance of two samples with high aspect ratio, demonstrating excellent bolometric performance. They were 2×8 μm^2 strips, measured in two different dilution refrigerators with base temperatures down to 60 and 30 mK. Above 60 mK, both samples demonstrated consistent results, even though they were evaluated in different measurement setups. In what follows, we analyze the data taken on sample A measured down to the lowest temperature, and present the performance of the reference sample (sample B) in the heat conductance measurements.

The experimental measurement setup is schematically presented in Fig. 1; essentially, we measure the heat conductance between the graphene electronic system and the substrate, using quantum interference–induced $R(T)$ as a thermometer for the graphene electronic system, assuming that the substrate temperature follows the base temperature of the cryostat. To monitor graphene resistance with good precision and minimal heat load, we used an rf scheme, suggested in Ref. [19]: relatively high graphene resistance was matched to the input resistance of a low-noise amplifier at a frequency of 650 MHz by a lumped-element resonator with quality factor $Q \approx 100$. A separate dc line allowed us to apply control power to the graphene sample [see Fig. 1(a)]. The rf scheme was accompanied by a dc measurement setup, which was also used for the bolometer calibration with heating at a known Joule power, while the electronic temperature of graphene was monitored by the rf conductance measurements. To avoid sample overheating by the rf probe power, we performed measurements at low rf powers—detailed information is presented in Sec. V and Appendixes H and I. The dc bias line was thermalized and filtered by thermocoax cable (https://www.thermocoax.com/) followed by lumped element filters; its thermalization was checked in separate experiments.

Figure 1(d) presents the calibration data for rf readout of the graphene electronic temperature: graphene resistance R and transmission resonance $S_{21,\min}$ were both measured as a function of the fridge temperature T. Cooperatively, $R(T)$ and $S_{21,\min}(T)$ define the minimum on transmission $S_{21,\min}$ as a function of graphene resistance $S_{21,\min}(R)$ [technically, both $R(T)$ and $S_{21,\min}(T)$ were interpolated with polynomials—see Appendixes C and D—to produce the $S_{21,\min}(T)$ functional dependence].

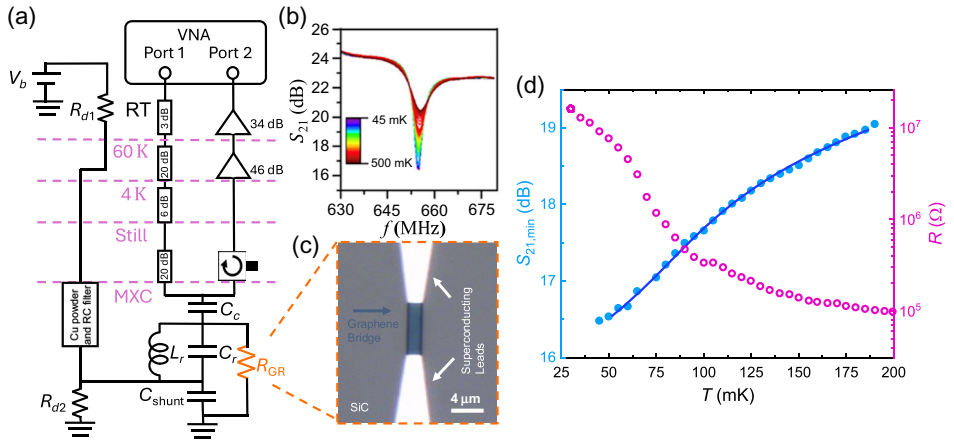

FIG. 1. Monitoring graphene electron temperature by radio frequency. (a) Cryogenic setup for rf notched transmission measurements on a graphene bridge. (b) A set of resonances on S_{21} transmission measured at different temperatures. The resonance quality factor follows the temperature dependence of graphene bridge resistance. (c) Optical transmission image of an 8×2 μm^2 graphene bridge, contacted by superconducting aluminum electrodes to eliminate electronic heat transport to the leads; the 8-μm-long graphene bridge suppresses undesired supercurrent due to the proximity effect. (d) Transmission S_{21} for monitoring the graphene resistance and electronic temperature. The minima on transmission $S_{21}(T)$ at resonance [(b)] vs the fridge temperature T (blue plot) and dc resistance measurements $R(T)$ made on the same bridge (red plot). Together, $R(T)$ and $S_{21}(T)$ establish one-to-one $S_{21}(T) \leftrightarrow R$ correspondence. Both $R(T)$ and $S_{21}(T)$ have a tendency to saturate at low temperatures—possibly due to improper thermalization (see the main text). VNA, vector network analyzer; MXC, mixing chamber.

III. BOLOMETRIC RESPONSE OF GRAPHENE SENSOR

With the thermometry setup calibrated [Fig. 1(d)], we applied a dc voltage to graphene terminals, overheating the strip, and measured the graphene electronic temperature in response to dc heating. The results are shown in Fig. 2(a), where we present graphene electronic temperature T_{gr} as a function of the dc bias voltage for different cryostat temperatures T. Note that as the bridge resistance diverges at $T \to 0$, for any given bias voltage V, the injected power $V^2/R \to 0$, so below some temperature the power dissipated on graphene becomes lower than uncontrolled heat

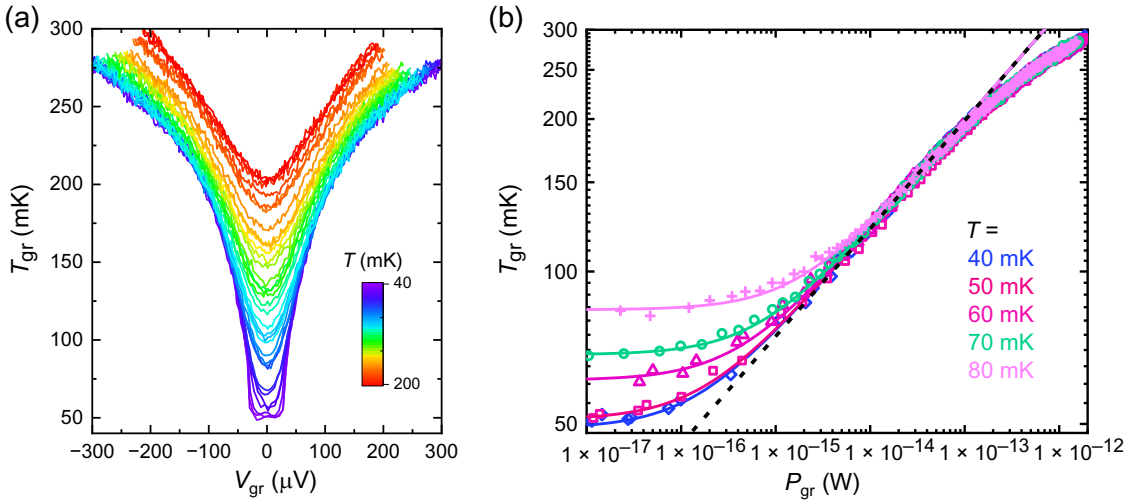

FIG. 2. (a) Graphene electronic temperature T_{gr} as a function of the dc bias voltage V_{gr}; a set of curves taken for different cryostat temperatures. (b) Same data presented as a function of the injected dc power $V_{gr}^2/R(T_{gr})$; only the data for the lowest fridge temperatures (45–80 mK) are presented for clarity. Symbols are for experimental data taken at cryostat temperatures of 40 mK (blue diamonds), 50 mK (red squares), 60 mK (magenta triangles), 70 mK (green circles), and 80 mK (violet crosses). The solid curves are fits to the power law $T_{gr} = (P_{gr}/\sigma + T_0^\beta)^{(1/\beta)}$ with $\beta = 4.7$, $\sigma = 2 \times 10^{-10}$ W/K$^\beta$, and $T_0 = 49.5$, 51.0, 61.0, 68.5, and 84.0 mK. The straight dashed black line has a slope of 4.7 ($P_{gr} \sim T_{gr}^{4.7}$).

flux from a nonthermalized environment (see Sec. V for details). This is why the $T_{gr}(V_{gr})$ curves taken at the lowest temperatures (50 mK or less) are flattened around the minima.

As the next step, we map the voltages on the horizontal axis onto dissipated powers: for any point (V_{gr}, T_{gr}) in Fig. 2(a), the calibration curve in Fig. 1(d) (blue) gives us the graphene temperature, and the corresponding dissipated power is thus $V_{gr}^2/R(T_{gr})$. The results of this transformation are presented in Fig. 2(b); only the plots for the lowest fridge temperatures are shown. Figure 2(b) shows the central plot of this contribution, which presents the bolometric response of the graphene device. Together with experimental data, Fig. 2(b) also presents fits to the standard bolometric equation $P_{gr} = \sigma(T_{gr}^{\beta} - T_0^{\beta})$ [20], which is based on the power balance condition between the graphene strip and its environment. If the environment is perfectly thermalized, T_0 matches the fridge temperature T, but it is not uncommon that below 100 mK the effective environment temperature does not follow T; see Sec. V for more details. For all fridge temperatures presented in Fig. 2(b) the fit, optimized for the intermediate power range 10^{-15}–10^{-13} W, returns the same values for the parameters $\sigma = 2 \times 10^{-10}$ W/K$^{\beta}$ and $\beta = 4.7$; at higher temperatures the exponent β slowly rises to 4.8 at 200 mK (more arguments in favor of $\beta \approx 5$ are presented in Appendix E). At zero power, the plots taken at 60 mK and above saturate to the fridge temperature, consistent with graphene being perfectly thermalized to the substrate. However, at lower temperatures, the graphene temperature saturates to 50 mK regardless of the fridge temperature (for a full dataset taken at different fridge temperatures, see Appendix F).

At high powers/temperatures, we observe a deviation from $T^{4.7}$ power dependence, apparently linked to the leakage of heat through quasiparticles in Al superconducting leads [21,22].

IV. ELECTRON-PHONON COUPLING AND NOISE EQUIVALENT POWER

Having the numbers for σ, β, and T_0 in $P_{gr} = \sigma(T_{gr}^{\beta} - T_0^{\beta})$, we produce a plot for thermal conductance $G_{th}(T_{gr}) = dP_{gr}/dT_{gr} = \beta\sigma T_{gr}^{(\beta-1)}$, presented in Fig. 3(a). The data for two graphene strips with the same geometry, 2×8 μm^2, were obtained in two different cryostats; although the lowest temperature was different in the two setups, we see that the thermal conductivity G_{th} in both experiments follows a universal power law $G_{th} \sim T^{3.7}$ [blue line in Fig. 3(a)]. The power law $G_{th} \sim T^{3.7}$ is consistent with the encouraging observation $P \sim T^{4.7}$, shown in Fig. 2(b). It has much stronger temperature dependence than previously reported electron-phonon couplings in graphene [10,23–28].

This observation correlates with another unexpected result, which is the observation of Arrhenius-type conductivity for $T < 200$ mK [Fig. 3(b)]. Altogether, the findings suggest that we reach new physics in the heat transfer process from the graphene electronic system to the substrate lattice. We attribute this heat transfer regime to the onset of strong localization of charge carriers at low temperatures, caused by quantum interference (see Fig. 7 in Appendix B) of the charge carriers in graphene in the presence of a

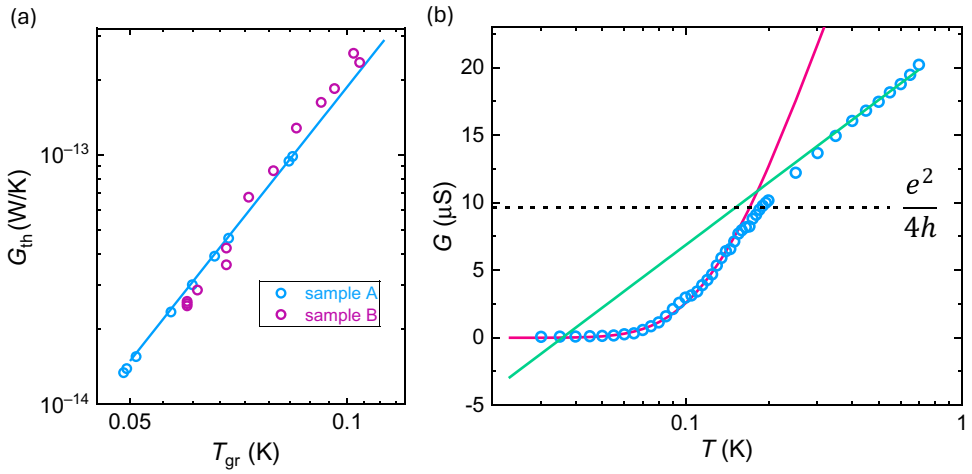

FIG. 3. (a) Graphene thermal conductance $G_{th}(T_{gr}) = \beta\sigma T_{gr}^{(\beta-1)}$ as a function of graphene temperature T_{gr}. Data are presented for two samples of identical dimensions $W \times L = 2 \times 8$ μm^2, measured in two different cryostats (with base temperatures of 30 mK for sample A and 60 mK for sample B). Both datasets have similar slope $\beta - 1 \approx 3.7$ in a log-log plot. The solid blue line is for the fit $G_{th}(T_{gr}) = 5\sigma T_{gr}^{3.7}$ with $\sigma = 2 \times 10^{-10}$ W/K$^{4.7}$. (b) Graphene conductance as a function of temperature. The red curve is a fit to the Arrhenius law $\ln(G_{gr}) = -E_{Arr}/(k_B T_{gr}) - 9.67$ with $E_{Arr} = k_B \times 0.32$ K. The green line presents the logarithmic dependence $(G_{\square}/4)(e^2/h)\ln((T/T'))$ with $G_{\square} = 0.69$ and $T' = 0.0358$ K. Transition from weak to strong localisation occurs at per square conductivity on the order of e^2/h (dashed black line), consistent with the interference-induced Anderson localization picture [15].

specific type of disorder [13–15]—such a scenario was mentioned in Refs. [29,30].

The unusual electron-phonon decoupling observed in this experiment has profound implications for the performance of graphene as a bolometer. The figure of merit for a bolometer is its noise equivalent power (NEP) [31,32], obtained from the standard formula NEP $= \sqrt{4k_B T_{gr}^2 G_{th}} \sim T_{gr}^{2.85}$. The measured electron–phonon coupling corresponds to an estimated of noise-equivalent power (NEP) of approximately 20 zW/$\sqrt{\text{Hz}}$ at $T =$ 40 mK. Below 40 mK, the estimated NEP of properly thermalized graphene would therefore surpass what is, to our knowledge, the best reported value of 20 zW/$\sqrt{\text{Hz}}$ [33].

V. DISCUSSION AND OUTLOOK

We have measured the electronic temperature of our graphene device with the rf transmission technique as a function of the dc power applied to graphene and estimated G_{th} from the data obtained. Applying a standard approach to evaluate the performance of the graphene bolometer in terms of NEP $= \sqrt{4k_B T^2 G_{th}}$, we estimate an expected NEP of approximately 20 zW/$\sqrt{\text{Hz}}$ at the cryostat base temperature of 40 mK (see Fig. 4, blue). However, the apparent saturation of the electronic temperature of graphene at 50 mK at low cryostat temperatures limits the NEP to approximately 50 zW/$\sqrt{\text{Hz}}$. This temperature saturation cannot be attributed to microwave heating or measurement artifacts. Even under conservative assumptions, the applied microwave excitation dissipates only about 14×10^{-18} W in graphene, corresponding to a negligible temperature increase of roughly 4.5 mK, which is too small to account for the observed saturation. A detailed analysis of this power estimation is provided in Appendix H. The saturation is therefore more likely caused by heat loading from nonthermalized environmental components, such as two-level fluctuators in the substrate dielectric and/or nonequilibrium quasiparticles in the aluminum leads. It is common knowledge that heat exchange with a nonthermalized environment leads to temperature saturation in engineered quantum devices at the level of 50–70 mK [34–43], consistent with our observations. An independent analysis of the dc V-I characteristics, presented in Appendix I, yields an estimated overheating power of 3×10^{-16} W. This value is in reasonable agreement with the power $\sigma T^{4.7} = 1.5 \times 10^{-16}$ W that would be injected from a nonthermalized environment at a temperature of 50 mK. Under proper thermalization conditions, the estimated NEP for 10 mK is 0.35 zW/$\sqrt{\text{Hz}}$, which is not far from the estimate made in our previous work [26]. The main difference between the measurements reported in Ref. [26] and the current measurements is the lower temperature range, providing an opportunity to convincingly reach the strong-localization regime, favoring better bolometric performance at low temperatures. We attribute this result to a synergistic effect of the onset of strong localization of charge carriers in graphene at low temperatures, caused by quantum interference of charge carriers, and a consequence of a better, lower-noise, less invasive graphene temperature readout, provided by the rf transmission scheme, implemented in this work. To get a better bolometric performance, we need to improve graphene thermalization at low temperatures, which, for a bolometric device, is especially challenging due to the otherwise beneficial, or even mandatory, thermal decoupling of the graphene bridge from the phonon bath.

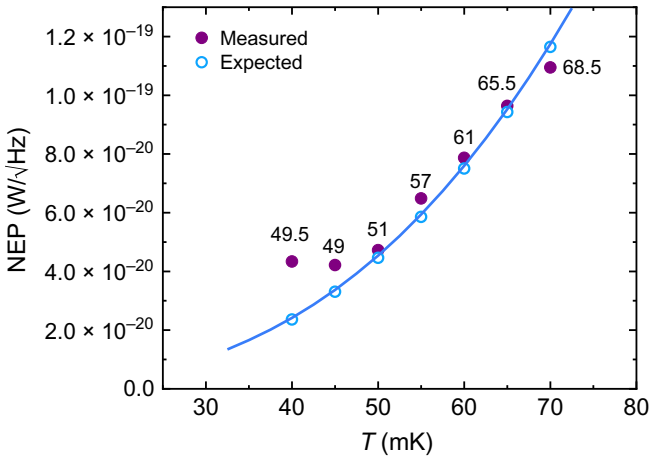

FIG. 4. NEP of the graphene bolometer as found experimentally (violet circles; the numbers next to violet circles are for the graphene electronic temperatures T_0—see Fig. 2) and as expected for the case of a graphene sample thermalized to the fridge temperature (blue circles). The blue line corresponds to $\sqrt{4k_B T^2 G_{th}}$ with $\beta = 4.7$ and $\sigma = 2 \times 10^{-10}$ W/K$^{4.7}$.

In view of prospective calorimetric applications [44], it is instructive to evaluate the heat capacity of the graphene bridge. The Fermi level in graphene is given by $E_F = \hbar v_F \sqrt{\pi n}$ [45,46]; for Fermi velocity $v_F = 1 \times 10^6$ m/s and for the carrier density $n = 10^{10}$ cm^{-2}, we arrive at $E_F/k_B = 122$ K. Assuming operation temperature $T = 50$ mK, we can estimate the number of electrons in a $k_B T$ slice around the Fermi level (the one contributing to the heat capacity) for $S = 2 \times 8$ μm^2 graphene bridge as $2(k_B T/E_F)nS \approx 1$. This is a quite remarkable result that shows that as a bolometric sensor, our graphene bridge is equivalent to a quantum dot with a single degree of freedom and heat capacity $C_e \approx k_B$. Therefore, the internal thermal response time of the graphene strip $(C/G_{Th}) = (2k_B nS/(5\sigma T^{2.7} T_F)) = 1.2$ ns at 50 mK, and in practical implementation of the calorimeter the bandwidth of the device readout scheme must be engineered to balance the trade-off between the device response time and sensitivity. The energy resolution is then [47,48] $\Delta E = \sqrt{k_B T^2 C_e} \approx$

$k_B T = 0.7 \times 10^{-24}$ J $= 0.7$ yJ, which corresponds to an energy of a single 1 GHz photon.

VI. CONCLUSIONS

We have demonstrated that a simple and scalable graphene micrometer-sized strip, cooled to millikelvin temperatures, offers zeptowatt sensitivity in a bolometric regime, thanks to its temperature-dependent resistance, caused by quantum interference effects, and thermal decoupling. This performance opens the path for scalable high-performance devices in quantum information technology, such as a click-detector resolving a single 1 GHz photon, or for effective realization of solid-state multichannel quantum tomography [49]. Moreover, our technology could be suitable to tackle challenges in cosmology and astronomy, fields where traditional detection of faint radiation has resulted in major breakthroughs [50]. Finally, the device core graphene bridge, hosting interacting two-dimensional electrons in a strongly localized regime, is a promising object for studies of thermalization dynamics of nonergodic many-body localized systems [51].

ACKNOWLEDGMENTS

This work at Chalmers University of Technology was jointly supported by the Chalmers Area of Advance Nano, Chalmers Area of Advanced Materials, 2D-TECH VINNOVA Competence Center (Grant No. 2019-00068), the Swedish Research Council (Grant No. 2021-05252), and the Knut and Alice Wallenberg Foundation via the Wallenberg Center for Quantum Technology. A.D. acknowledges support from the Horizon Europe EIC Pathfinder project IQARO (Grant Agreement No. 101115190). Sample fabrication and analysis were supported by Myfab Chalmers and the Chalmers Materials Analysis Laboratory. This work at Aalto University was supported by Research Council of Finland Centre of Excellence program Grants No 336810 and No. 349601 (THEPOW). We acknowledge the facilities and technical support of Otaniemi Research Infrastructure for Micro and Nanotechnologies to perform this research. B.K. acknowledges the European Union's Horizon Europe research and innovation program under Marie Skłodowska-Curie Grant Agreement No. 101150440 (TcQTD). We are grateful for discussions with Floriana Lombardi, Dmitry S. Golubev, Igor V. Lerner, and Tord Claeson.

DATA AVAILABILITY

The data that support the findings of this article are openly available [52].

APPENDIX A: CHIP LAYOUT

Four identical chips with an approximate size of 3.5×3.5 mm^2 were fabricated on a silicon carbide/epigraphene wafer with dimensions of 7×7 mm^2, doped to a low carrier density, and cut into individual chips. Each chip contained four sets of graphene strips with different aspect ratios, contacted by superconducting aluminum and three Hall bars for monitoring the carrier density in graphene; see Fig. 5.

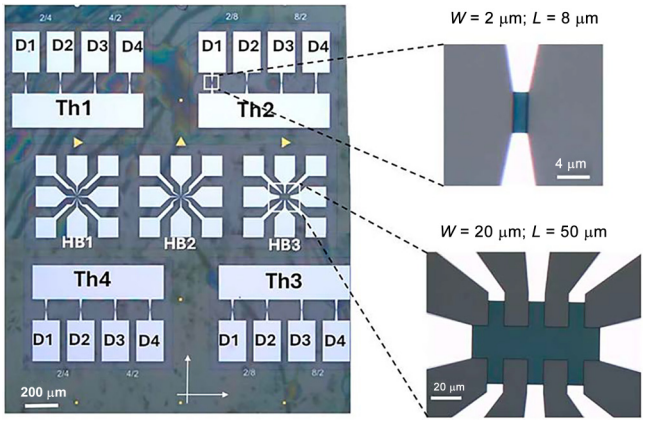

FIG. 5. Chip layout: reflection image in an optical microscope. One of the graphene strips (2×8 μm^2) is shown, together with the Hall bar HB3, which was examined for magnetotransport. Bright leads represent the Al film.

APPENDIX B: MAGNETOTRANSPORT MEASUREMENTS

The performance of one of the four chips described in Appendix A was evaluated in a separate cryostat, demonstrating a quantum Hall plateau at fields of around 1 T, and a carrier density of 4×10^{10} cm^{-2}; the corresponding magnetotransport data are shown in Fig. 6. The chip described in this work was measured in a dilution refrigerator with a magnetic field of 0.2 T; the results are presented in Fig. 7. Despite an apparent R_{xx}-R_{xy} mixing at low fields, where the sample resistance increases due to quantum interference, the slope of the R_{xy} plot of 29.5 kΩ/T confirms that the carrier density remains low, on the order of 10^{10} cm^{-2}.

APPENDIX C: $S_{21}(T)$ CALIBRATION PLOT

Here we illustrate a polynomial fit for $S_{21}(T)$. Transmission S_{21} at $V_{\text{bias}} = 0$ was measured separately with a long averaging time at fridge temperatures in the range 40–200 mK to produce the calibration plot $S_{21} \to T_{\text{gr}}$ shown in Fig. 8.

APPENDIX D: $R(T)$ CALIBRATION PLOT

Here we illustrate our interpolation of $R(T)$. The graphene resistance was measured in direct current at zero bias voltage as a function of the fridge temperature (at zero bias voltage); see Fig. 9.

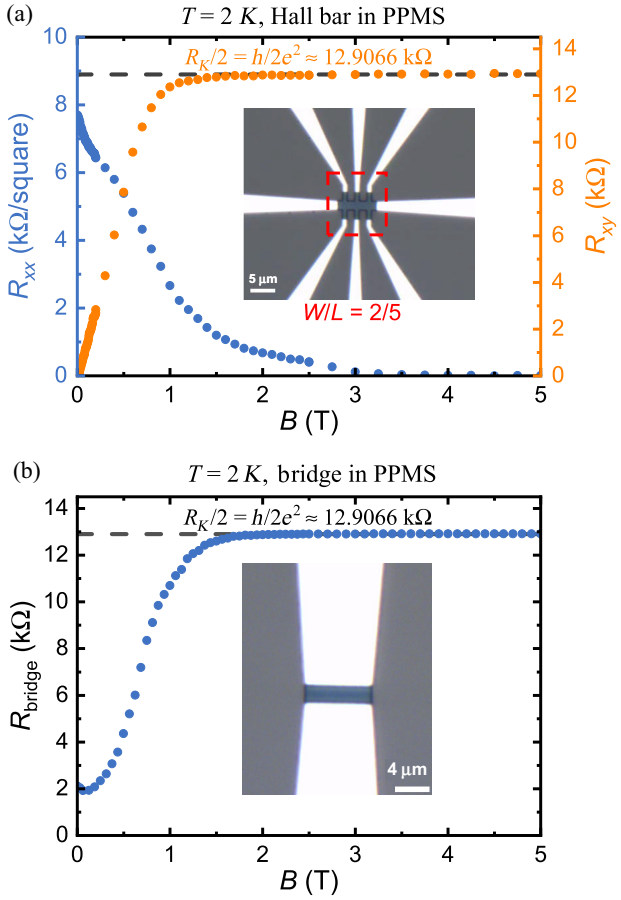

FIG. 6. Magnetotransport data taken on a test sibling device in a separate cryostat. (a) Data obtained for a Hall bar marked by a red square in the chip image (see the inset). (b) Two-point measurements on a graphene bridge—see the inset image. From these measurements, we extracted a carrier density of approximately 4×10^{10} cm^{-2} for the sibling device. The appearance of well-defined quantized Hall values confirms that the material is genuine monolayer graphene, as the observed plateaus correspond to the anomalous quantum Hall sequence characteristic of graphene. The fact that the two-terminal measurement on the Hall bar yields the correct quantized resistance also indicates that the metal-graphene contact resistance is negligible at this level.

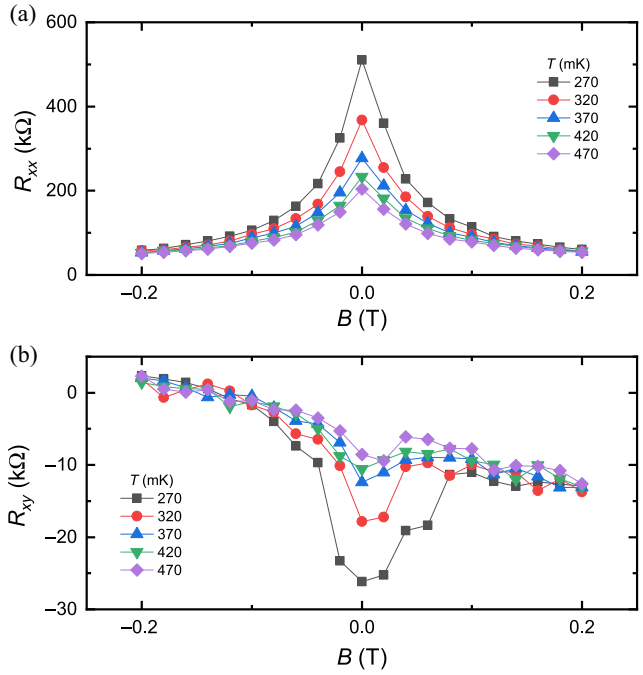

FIG. 7. Magnetotransport measurements on graphene Hall bar HB3, taken at several temperatures: 270, 320, 370, 420, and 470 mK. (a) $R_{xx}/\square(B)$ plot, demonstrating delocalization of graphene charge carriers in a magnetic field, breaking time-reversal symmetry. (b) R_{xy} measured on the same Hall bar: an obvious mixing of R_{xy} and R_{xx} at zero field is present, but an overall slope of -39.5 kΩ/T can be seen, which is consistent with the estimate of the carrier density of 1.6×10^{10} cm^{-2}.

APPENDIX E: GRAPHENE TEMEPRATURE VERSUS HEATING POWER: $P_{gr} \sim T_{gr}^5$ VERSUS $P_{gr} \sim T_{gr}^5$

Here we compare two exponents in the power-temperature dependence. To evaluate the exponent β in $P_{gr} \sim T_{gr}^{\beta}$, we plot T_{gr}^5 and T_{gr}^4 versus the dissipated power P_{gr} in Fig. 10. We see that for $T_{gr}^5(P_{gr})$ all the data points are aggregated along the straight line, suggesting that β is close to 5.

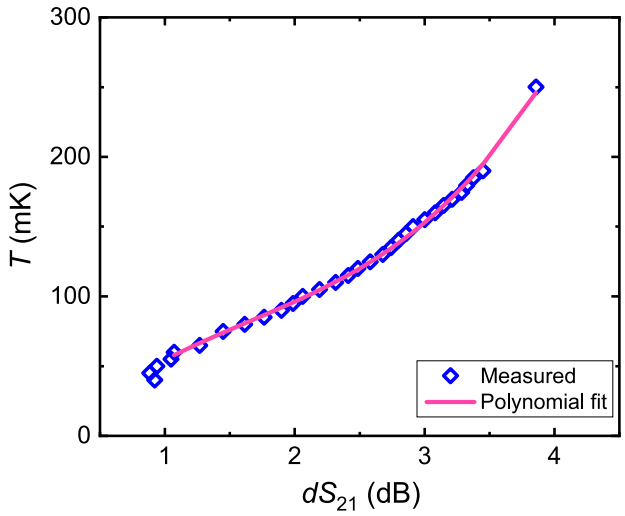

FIG. 8. $S_{21} \rightarrow T_{gr}$ calibration plot. The calibration curve is the best polynomial fit $T_{gr}(S_{21}) = a(dS_{21})^3 + b(dS_{21})^2 + c(dS_{21}) + d$, where $dS_{21} = S_{21} - 15.6$ dB, $a = 0.00715$, $b = -0.03543$, $c = 0.09803$, and $d = -0.01529$. The polynomial fit was performed over temperatures in the range from 60 to 200 mK to exclude the region where the sample temperature saturates.

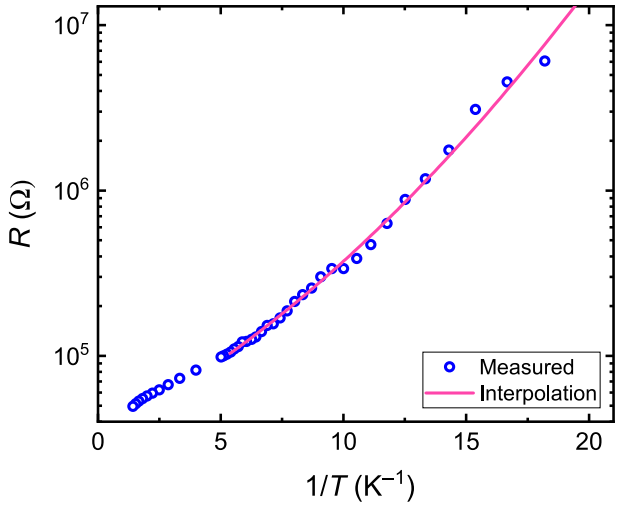

FIG. 9. Graphene resistance R vs temperature T. The interpolation curve is given by $\ln R = a/T^2 + b/T + c$, where $a = 0.00701$, $b = 0.1703$, and $c = 10.43$.

APPENDIX F: GRAPHENE TEMPERATURE VERSUS HEATING POWER: FULL DATASET

While in the main text we concentrate on the performance of the graphene bolometer at a few selected temperatures, in Fig. 11 we present the full set of acquired data. As $P_{gr} \to 0$, the plots saturate at the corresponding T. For temperatures in the range $T < T_{gr} \lesssim 200$ mK, the plots

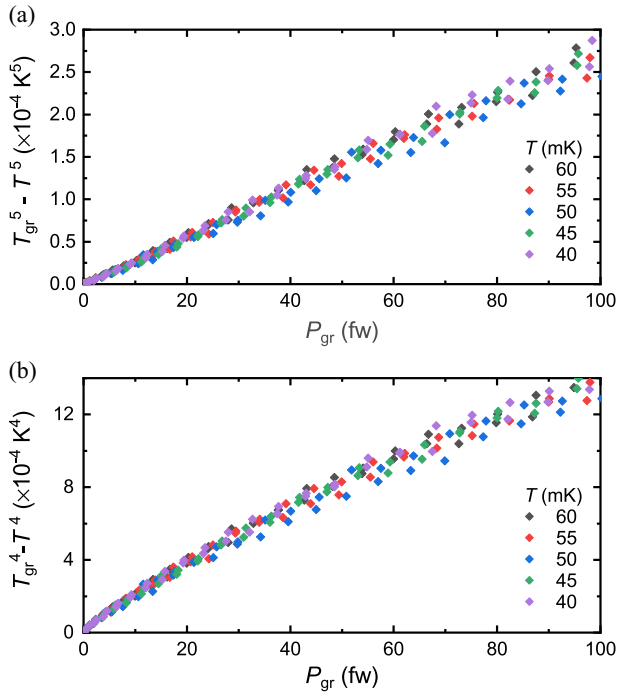

FIG. 10. Graphene temperature T_{gr} to the (a) fifth and (b) fourth power vs the power P_{gr} dissipated in graphene. Note the linear dependence in (a).

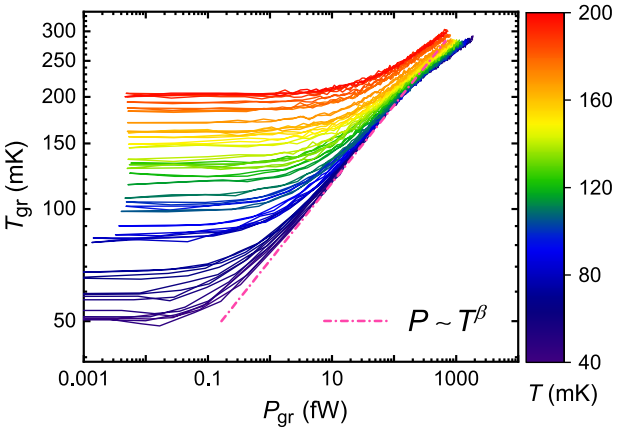

FIG. 11. Graphene temperature T_{gr} vs heating power P_{gr} for different fridge temperatures T.

reveal the dependence of $P_{gr} \sim T_{gr}^5$; above $T_{gr} \approx 200$ mK, there seems to be a crossover to a different slope. We speculate that the temperature of 200 mK corresponds to the onset of heat conductance through quasiparticles in Al electrodes.

APPENDIX G: GRAPHENE TEMPERATURE SATURATION AT LOW FRIDGE TEMPERATURES

The plots in Fig. 12 show in more detail the overheating of the graphene bolometer due to a nonthermalized

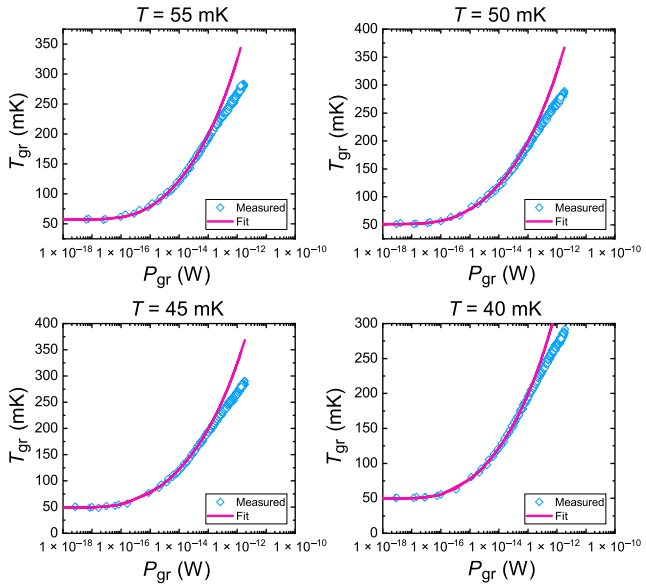

FIG. 12. Experimental data for T_{gr} vs P_{gr} (diamonds) for fridge temperatures $T = 55$, 50, 45, and 40 mK. Solid lines are fits to $T_{gr} = ((P_{gr}/A) + T_0^5)^{1/5}$ with the same $A = 3.5 \times 10^{-10}$ W for all plots. The saturation temperatures $T_0 = \lim_{P_{gr} \to 0} T_{gr}$ extracted from the fits are 57, 51, 49, and 49.5 mK.

environment, resulting in graphene temperature saturation above the fridge temperature at low dissipation powers.

APPENDIX H: EFFECT OF THE MICROWAVE MEASUREMENT POWER: UPPER-BOUND ESTIMATION

Here we discuss the details of the thermalization for the measurement leads and possible effects of the microwave excitation power, used in our thermometric setup. The proper thermalization of microwave lines is ensured by a set of attenuators on the input channel and a double-junction isolator (34 dB) at the output. All measurements presented were done with a vector network analyzer output power of -60 dBm; with 46 dB provided by attenuators and accounting for an extra 7 dB loss in the combiner (3 dB) and cables (4 dB), we arrive at the excitation power on a tank circuit of -113 dBm. At 50 mK, the tank circuit is essentially in a critically coupled regime: the S_{21} resonance is 7.5 dB deep [see Fig. 1(b)]. For a critically coupled resonator, the power $P_{\rm diss}$ dissipated in the resonator is half the excitation power, i.e., -116 dBm (2.5 fW). However, only a small fraction of this power $\alpha = R_Q/R_{\rm gr}$ is absorbed by graphene, where $R_{\rm gr}$ is the graphene resistance (7.63 MΩ at 50 mK) and $R_Q = Q_i\sqrt{L/C}$ is the equivalent dissipative resistance of the resonance circuit. Given the tank circuit parameters $Q_i = 440$ [for a critically coupled resonator $Q_i = 2f/\Delta f$, and the linewidth Δf is shown in Fig. 1(b)], $L = 47$ nH, and $C = 1$ pF (by design), we arrive at $R_Q = 95$ kΩ and $\alpha = 0.012$. The heat conductance $G_{\rm th} = 1.45 \times 10^{-14}$ W/K is known from Fig. 3(a), so we can estimate the overheating due to the measurement power as $\Delta T_{\rm gr} = (\alpha P_{\rm diss}/G_{\rm th}) = 1.5$ mK at a fridge temperature of 50 mK. Reiterating these calculations for all the relevant temperatures, we produce Fig. 13 for $\Delta T_{\rm gr}$ at different fridge temperatures. We see that at, say, 40 mK, the overheating due to the measurement power does not exceed 2.5 mK, and therefore could not account for the observed graphene temperature saturation to 50 mK.

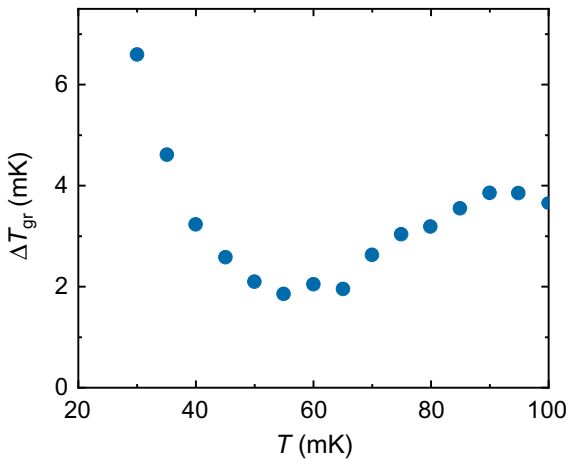

FIG. 13. Upper-bound estimation for the graphene overheating due to the microwave measurement power for different fridge temperatures T.

APPENDIX I: VOLTAGE-CURRENT CURVES MEASURED ON DIRECT CURRENT: MODEL PREDICTION VERSUS MEASUREMENTS

We now substantiate the main underlying assumption of our model: that the power-resistance relation of the graphene bridge arises solely from the bolometric effect, and no intrinsic nonlinearity (due to, for example, Coulomb blockade effects) is involved. Using graphene bridge parameters extracted from microwave measurements, we reconstruct the expected $V-I$ characteristics and show that they agree with the experimental data. The procedure is as follows. First, the graphene temperature $T_{\rm gr}$ is set equal to the refrigerator temperature. The graphene resistance R is then obtained from the polynomial calibration $\ln R = (a/T^2) + (b/T) + c$ (see Fig. 9). For a given dc bias I, the dissipated power in graphene is calculated as $P_{\rm gr} = RI^2$. The resulting electron overheating is determined from the thermal balance relation, yielding an updated graphene temperature $T'_{\rm gr} = ((P_{\rm gr}/\sigma) + T_{\rm gr}^{\beta})^{(1/\beta)}$. We iterate the procedure until a self-consistent solution satisfying $T'_{\rm gr}(I) = T_{\rm gr}(I)$ is obtained. The results of these calculations are presented in Fig. 14 as a set of $T_{\rm gr}(I)$ plots corresponding to different fridge temperatures.

Finally, we use the same $\ln(R)$ calibration to convert the plots for $T_{\rm gr}$ into corresponding V-I plots $V = R(T_{\rm gr}(I))I$ as shown in Fig. 15.

We find that at 60 mK and above, the theory closely matches the experiment. However, at 40 mK and below, the experimental curves develop a region with negative

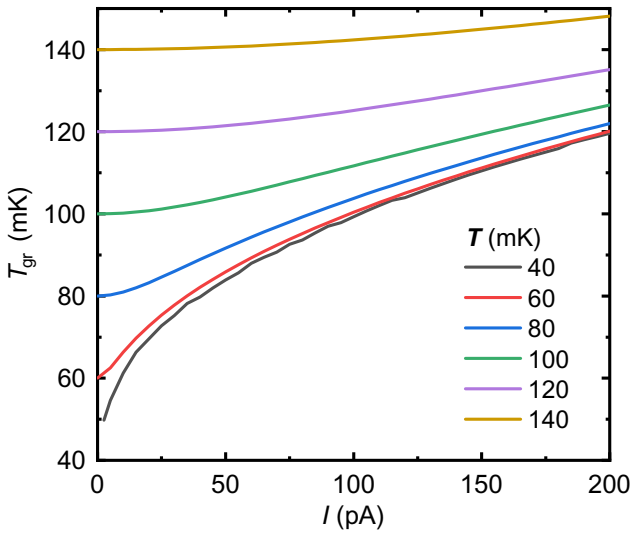

FIG. 14. Graphene temperature $T_{\rm gr}$ as a function of dc bias I for different fridge temperatures T.

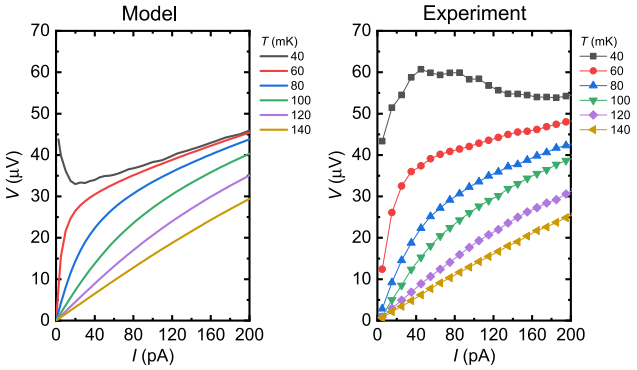

FIG. 15. Calculated (left) and measured (right; symbols correspond to experimental data, and lines are guides for the eye) *V*-*I* curves at different fridge temperatures *T*.

dV/dI, and the model fails to reproduce this behavior. We speculate that this discrepancy arises from strong fluctuations of graphene temperature at low refrigerator temperatures. In our model, the $R(T)$ calibration connects two time-averaged quantities: the average graphene temperature $\langle T_{\rm gr}(t)\rangle_t$ and the average graphene resistance $\langle R(t)\rangle_t$. This approach is valid only when the temperature fluctuations $\delta T(t)$ are small $\langle \delta T(t)\rangle_t \ll \langle T_{\rm gr}(t)\rangle_t$. If the fluctuations become large, the relation $\langle \ln(R)\rangle_t = a/\langle T(t)\rangle_t^2 + b/\langle T(t)\rangle_t + c$ no longer holds, and the calibration needs to be revised. We leave this refinement to future work on the graphene calorimeter.

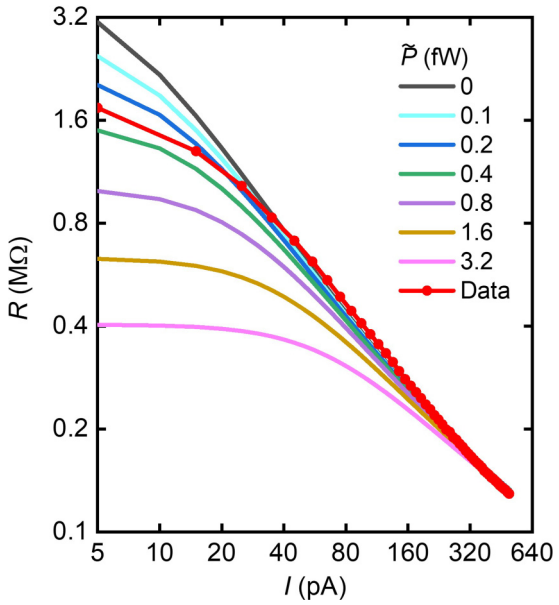

FIG. 16. Effect of the background heating power $\tilde{P}$ on the shape of graphene resistance $R(I) = V/I$ vs bias current curves. A set of theoretical curves and experimental data (red circles correspond to experimental data, and the red curve is a guide for the eye) at the fridge temperature of 60 mK.

Nevertheless, we can still use the model at 60 mK to estimate an upper bound on the uncontrolled heating power (e.g., from wiring losses or nonthermalized radiation shields). Figure 16 shows a set of V/I versus I curves, calculated for different assumed heating powers $\tilde{P}$.

As evident from Fig. 16, an external heating reduces the V/I value at zero current bias and introduces a flat (zero-slope) region. Comparing the theory plots versus experiment, we deduce 3×10^{-16} W as an upper limit for uncontrolled external heating. Although the source of overheating cannot be directly inferred from the data in Fig. 16, we can make a crucial observation: the power injected by the substrate at a temperature of 50 mK is $\sigma(50\ \text{mK})^{4.7} = 1.5 \times 10^{-16}$ W. Thus, two independent experiments—graphene temperature measurements in a microwave setup and dc *V*-*I* measurements—yield values of $\tilde{P}$ and $T_{\rm gr}$ that satisfy the relation $\tilde{P} = \sigma T^{4.7}$ (within a factor of 2). This observation strongly favors the overheating scenario suggested by a nonthermalised substrate.

[1] C. M. Adair *et al.*, Search for dark matter axions with CAST-CAPP, Nat. Commun. **13**, 6180 (2022).

[2] T. Braine *et al.* (ADMX Collaboration), Extended search for the invisible axion with the axion dark matter experiment, Phys. Rev. Lett. **124**, 101303 (2020).

[3] A. L. Pankratov, A. V. Gordeeva, A. V. Chiginev, L. S. Revin, A. V. Blagodatkin, N. Crescini, L. S. Kuzmin, Detection of single-mode thermal microwave photons using an underdamped Josephson junction, Nat. Commun. **16**, 3457 (2025).

[4] I. G. Irastorza and J. Redondo, New experimental approaches in the search for axion-like particles, Prog. Part. Nucl. Phys. **102**, 89 (2018).

[5] P. Sikivie, Experimental tests of the invisible axion, Phys. Rev. Lett. **51**, 1415 (1983).

[6] T. M. Shokair, J. Root, K. A. Van Bibber, B. Brubaker, Y. V. Gurevich, S. B. Cahn, S. K. Lamoreaux, M. A. Anil, K. W. Lehnert, B. K. Mitchell, A. Reed, and G. Carosi, Future directions in the microwave cavity search for dark matter axions, Int. J. Mod. Phys. A **29**, 1443004 (2014).

[7] B. Karimi and J. P. Pekola, Quantum trajectory analysis of single microwave photon detection by nanocalorimetry, Phys. Rev. Lett. **124**, 170601 (2020).

[8] A. M. Gunyhó, S. Kundu, J. Ma, W. Liu, S. Niemelä, G. Catto, V. Vadimov, V. Vesterinen, P. Singh, Q. Chen, and M. Möttönen, Single-shot readout of a superconducting qubit using a thermal detector, Nat. Electron. **7**, 288 (2024).

[9] C. B. McKitterick, D. E. Prober, H. Vora, and X. Du, Ultrasensitive graphene far-infrared power detectors, J. Phys.: Condens. Matter **27**, 164203 (2015).

[10] D. K. Efetov and P. Kim, Controlling electron-phonon interactions in graphene at ultrahigh carrier densities, Phys. Rev. Lett. **105**, 256805 (2010).

[11] R. Kokkoniemi, J.-P. Girard, D. Hazra, A. Laitinen, J. Govenius, R. E. Lake, I. Sallinen, V. Vesterinen, M. Partanen, J. Y. Tan, K. W. Chan, K. Y. Tan, P. Hakonen, and M.

Möttönen, Bolometer operating at the threshold for circuit quantum electrodynamics, Nature **586**, 47 (2020).

[12] H. He, K. Cedergren, N. Shetty, S. Lara-Avila, S. Kubatkin, T. Bergsten, and G. Eklund, Accurate graphene quantum Hall arrays for the new International System of Units, Nat. Commun. **13**, 6933 (2022).

[13] E. McCann, K. Kechedzhi, V. I. Fal'ko, H. Suzuura, T. Ando, and B. L. Altshuler, Weak-localization magnetoresistance and valley symmetry in graphene, Phys. Rev. Lett. **97**, 146805 (2006).

[14] S. Lara-Avila, A. Tzalenchuk, S. Kubatkin, R. Yakimova, T. J. B. M. Janssen, K. Cedergren, T. Bergsten, and V. Fal'ko, Disordered Fermi liquid in epitaxial graphene from quantum transport measurements, Phys. Rev. Lett. **107**, 166602 (2011).

[15] L. A. Ponomarenko, A. K. Geim, A. A. Zhukov, R. Jalil, S. V. Morozov, K. S. Novoselov, I. V. Grigorieva, E. H. Hill, V. V. Cheianov, V. I. Fal'ko, K. Watanabe, T. Taniguchi, and R. V. Gorbachev, Tunable metal–insulator transition in double-layer graphene heterostructures, Nat. Phys. **7**, 958 (2011).

[16] M. L. Roukes, Yoctocalorimetry: Phonon counting in nanostructures, Phys. B: Condens. Matter **263–264**, 1 (1999).

[17] N. Shetty, H. He, R. Mitra, J. Huhtasaari, K. Iordanidou, J. Wiktor, S. Kubatkin, S. P. Dash, R. Yakimova, L. Zeng, E. Olsson, and S. Lara-Avila, Scalable fabrication of edge contacts to 2D materials: Implications for quantum resistance metrology and 2D electronics, ACS Appl. Nano Mater. **6**, 6292 (2023). publisher: American Chemical Society.

[18] H. He, K. H. Kim, A. Danilov, D. Montemurro, L. Yu, Y. W. Park, F. Lombardi, T. Bauch, K. Moth-Poulsen, T. Iakimov, R. Yakimova, P. Malmberg, C. Müller, S. Kubatkin, and S. Lara-Avila, Uniform doping of graphene close to the Dirac point by polymer-assisted assembly of molecular dopants, Nat. Commun. **9**, 3956 (2018).

[19] R. J. Schoelkopf, P. Wahlgren, A. A. Kozhevnikov, P. Delsing, and D. E. Prober, The radio-frequency single-electron transistor (RF-SET): A fast and ultrasensitive electrometer, Science **280**, 1238 (1998).

[20] V. F. Gantmakher, The experimental study of electron-phonon scattering in metals, Rep. Prog. Phys. **37**, 317 (1974).

[21] S. Battisti, G. De Simoni, A. Braggio, A. Paghi, L. Sorba, and F. Giazotto, Extremely weak sub-kelvin electron–phonon coupling in InAs on insulator, Appl. Phys. Lett. **125**, 202601 (2024).

[22] K. L. Viisanen and J. P. Pekola, Anomalous electronic heat capacity of copper nanowires at sub-Kelvin temperatures, Phys. Rev. B **97**, 115422 (2018).

[23] A. C. Betz, F. Vialla, D. Brunel, C. Voisin, M. Picher, A. Cavanna, A. Madouri, G. Fève, J.-M. Berroir, B. Plaçais, and E. Pallecchi, Hot electron cooling by acoustic phonons in graphene, Phys. Rev. Lett. **109**, 056805 (2012).

[24] I. V. Borzenets, U. C. Coskun, H. T. Mebrahtu, Y. V. Bomze, A. I. Smirnov, and G. Finkelstein, Phonon bottleneck in graphene-based Josephson junctions at millikelvin temperatures, Phys. Rev. Lett. **111**, 027001 (2013).

[25] S. Lara-Avila, A. Danilov, D. Golubev, H. He, K. H. Kim, R. Yakimova, F. Lombardi, T. Bauch, S. Cherednichenko, and S. Kubatkin, Towards quantum-limited coherent detection of terahertz waves in charge-neutral graphene, Nat. Astron. **3**, 983 (2019).

[26] B. Karimi, H. He, Y. C. Chang, L. Wang, J. P. Pekola, R. Yakimova, N. Shetty, J. T. Peltonen, S. Lara-Avila, and S. Kubatkin, Electron-phonon coupling of epigraphene at millikelvin temperatures measured by quantum transport thermometry, Appl. Phys. Lett. **118**, 103102 (2021).

[27] A. El Fatimy, R. L. Myers-Ward, A. K. Boyd, K. M. Daniels, D. K. Gaskill, and P. Barbara, Epitaxial graphene quantum dots for high-performance terahertz bolometers, Nat. Nanotechnol. **11**, 335 (2016).

[28] A. El Fatimy, P. Han, N. Quirk, L. St. Marie, M. T. Dejarld, R. L. Myers-Ward, K. Daniels, S. Pavunny, D. K. Gaskill, Y. Aytac, T. E. Murphy, and P. Barbara, Effect of defect-induced cooling on graphene hot-electron bolometers, Carbon **154**, 497 (2019).

[29] G. McArdle and I. V. Lerner, Electron-phonon decoupling in two dimensions, Sci. Rep. **11**, 24293 (2021).

[30] W. Chen and A. A. Clerk, Electron-phonon mediated heat flow in disordered graphene, Phys. Rev. B **86**, 125443 (2012).

[31] F. J. Low, Low-temperature germanium bolometer, J. Opt. Soc. Am. **51**, 1300 (1961).

[32] P. L. Richards, Bolometers for infrared and millimeter waves, J. Appl. Phys. **76**, 1 (1994).

[33] R. Kokkoniemi, J. Govenius, V. Vesterinen, R. E. Lake, A. M. Gunyhó, K. Y. Tan, S. Simbierowicz, L. Grönberg, J. Lehtinen, M. Prunnila, J. Hassel, A. Lamminen, O.-P. Saira, and M. Möttönen, Nanobolometer with ultralow noise equivalent power, Commun. Phys. **2**, 1 (2019).

[34] X. Y. Jin, A. Kamal, A. P. Sears, T. Gudmundsen, D. Hover, J. Miloshi, R. Slattery, F. Yan, J. Yoder, T. P. Orlando, S. Gustavsson, and W. D. Oliver, Thermal and residual excited-state Population in a 3D transmon qubit, Phys. Rev. Lett. **114**, 240501 (2015).

[35] A. Kulikov, R. Navarathna, and A. Fedorov, Measuring effective temperatures of Qubits using correlations, Phys. Rev. Lett. **124**, 240501 (2020).

[36] A. Sultanov, M. Kuzmanović, A. V. Lebedev, and G. S. Paraoanu, Protocol for temperature sensing using a three-level transmon circuit, Appl. Phys. Lett. **119**, 144002 (2021).

[37] D. S. Lvov, S. A. Lemziakov, E. Ankerhold, J. T. Peltonen, and J. P. Pekola, Thermometry based on a superconducting qubit, Phys. Rev. Appl. **23**, 054079 (2025).

[38] H. Paik, D. I. Schuster, L. S. Bishop, G. Kirchmair, G. Catelani, A. P. Sears, B. R. Johnson, M. J. Reagor, L. Frunzio, L. I. Glazman, S. M. Girvin, M. H. Devoret, and R. J. Schoelkopf, Observation of high coherence in Josephson junction qubits measured in a three-dimensional circuit QED architecture, Phys. Rev. Lett. **107**, 240501 (2011).

[39] J. Burnett, L. Faoro, I. Wisby, V. L. Gurtovoi, A. V. Chernykh, G. M. Mikhailov, V. A. Tulin, R. Shaikhaidarov, V. Antonov, P. J. Meeson, A. Y. Tzalenchuk, and T. Lindström, Evidence for interacting two-level systems from the $1/f$ noise of a superconducting resonator, Nat. Commun. **5**, 4119 (2014).

[40] S. E. de Graaf, L. Faoro, J. Burnett, A. A. Adamyan, A. Y. Tzalenchuk, S. E. Kubatkin, T. Lindström, and A. V. Danilov, Suppression of low-frequency charge noise in superconducting resonators by surface spin desorption, Nat. Commun. **9**, 1143 (2018).

[41] M. Lucas, A. V. Danilov, L. V. Levitin, A. Jayaraman, A. J. Casey, L. Faoro, A. Y. Tzalenchuk, S. E. Kubatkin, J. Saunders, and S. E. de Graaf, Quantum bath suppression in a superconducting circuit by immersion cooling, Nat. Commun. **14**, 3522 (2023).

[42] S. E. de Graaf, A. A. Adamyan, T. Lindström, D. Erts, S. E. Kubatkin, A. Y. Tzalenchuk, and A. V. Danilov, Direct identification of dilute surface spins on Al_2O_3: Origin of flux noise in quantum circuits, Phys. Rev. Lett. **118**, 057703 (2017).

[43] C. M. Quintana *et al.*, Observation of classical-quantum crossover of $1/f$ flux noise and its paramagnetic temperature dependence, Phys. Rev. Lett. **118**, 057702 (2017).

[44] C. D. Satrya, Y.-C. Chang, A. S. Strelnikov, R. Upadhyay, I. K. Mäkinen, J. T. Peltonen, B. Karimi, and J. P. Pekola, Thermal spectrometer for superconducting circuits, Nat. Commun. **16**, 4435 (2025).

[45] A. H. Castro Neto, F. Guinea, N. M. R. Peres, K. S. Novoselov, and A. K. Geim, The electronic properties of graphene, Rev. Mod. Phys. **81**, 109 (2009).

[46] S. Das Sarma, S. Adam, E. H. Hwang, and E. Rossi, Electronic transport in two-dimensional graphene, Rev. Mod. Phys. **83**, 407 (2011).

[47] S. H. Moseley, J. C. Mather, and D. McCammon, Thermal detectors as X-ray spectrometers, J. Appl. Phys. **56**, 1257 (1984).

[48] G.-H. Lee, D. K. Efetov, W. Jung, L. Ranzani, E. D. Walsh, T. A. Ohki, T. Taniguchi, K. Watanabe, P. Kim, D. Englund, and K. C. Fong, Graphene-based Josephson junction microwave bolometer, Nature **586**, 42 (2020).

[49] L. Pereira, J. J. García-Ripoll, and T. Ramos, Parallel tomography of quantum non-demolition measurements in multi-qubit devices, npj Quantum Inf. **9**, 1 (2023).

[50] F. Paolucci, N. Ligato, G. Germanese, V. Buccheri, and F. Giazotto, Fully superconducting Josephson bolometers for gigahertz astronomy, Appl. Sci. **11**, 746 (2021).

[51] M. Ueda, Quantum equilibration, thermalization and prethermalization in ultracold atoms, Nat. Rev. Phys. **2**, 669 (2020).

[52] Y.-C. Chang, F. Chianese, N. Shetty, J. Huhtasaari, A. Jayaraman, J. Peltonen, S. Lara-Avila, B. Karimi, A. Danilov, J. Pekola, and S. Kubatkin, Data for quantum-ready microwave detection with scalable graphene bolometers in the strong localization regime, Zenodo, 2026, https://doi.org/10.5281/zenodo.19550276.